Available online at www.sciencedirect.com
ScienceDirect
International Journal of Heat and Mass Transfer 50 (2007) 4039–4051
International Journal of HEAT and MASS TRANSFER
www.elsevier.com/locate/ijhmt

CHF model for subcooled flow boiling in Earth gravity and microgravity

Hui Zhang [a], Issam Mudawar [a,*], Mohammad M. Hasan [b]

[a] Boiling and Two-phase Flow Laboratory, School of Mechanical Engineering, Purdue University, 585 Purdue Mall, West Lafayette, IN 47907, USA
[b] NASA Glenn Research Center, 21000 Brookpark Road, Cleveland, OH 44135, USA

Received 8 September 2006; received in revised form 26 January 2007
Available online 27 March 2007

Abstract

This study is the first attempt at extending the Interfacial Lift-off CHF Model to subcooled flow boiling conditions. A new CHF database was generated for FC-72 from ground tests as well as from microgravity tests that were performed in parabolic flight trajectory. These tests also included high-speed video imaging and analysis of the liquid–vapor interface during the CHF transient. Both the CHF data and the video records played a vital role in constructing and validating the extended CHF model. The fundamental difference between the original Interfacial Lift-off Model, which was developed for saturated flow boiling, and the newly extended model is the partitioning of wall energy between sensible and latent heat for subcooled flow boiling. This partitioning is modeled with the aid of a new "heat utility ratio". Using this ratio, the extended Interfacial Lift-off Model is shown to effectively predict both saturated and subcooled flow boiling CHF in Earth gravity and in microgravity.

1. Introduction

Subcooled flow boiling is a highly efficient means of removing heat from high-heat-flux dissipating surfaces. It is used in cooling nuclear reactor cores and absorbing heat from combustion products in power plant boilers. In recent years, thermal management needs in the electronics and aerospace industries have spurred unprecedented interest in implementing flow boiling to capitalize upon its potential to produce large heat transfer coefficients.

This important attribute has also been a primary reason for recent intense efforts to utilize flow boiling in a broad variety of future space systems and subsystems, including Rankine cycle power generation, electronic cooling, life support, and waste management. With the significant enhancement in heat transfer coefficient compared to single-phase cooling, flow boiling is expected to yield order-of-magnitude reduction in weight-to-heat-load ratio, which is a primary goal in the design of space systems.

Like most boiling systems, heat removal in space is limited by the critical heat flux (CHF). Exceeding this limit causes a substantial decrease in the heat transfer coefficient, which, for heat-flux controlled surfaces, can trigger serious physical damage to the surface being cooled. Accurate CHF prediction is therefore crucial to the design and safety analysis of flow boiling systems.

Flow boiling CHF has been explored extensively since the 1940s. For the most part, CHF determination has relied on empirical correlations. Those correlations are valid for the specific geometries and operating conditions of the experiments upon which they are based. Due to the dependence of CHF on a relatively large number of parameters (geometry, pressure, flow rate, subcooling, etc.), and given the limited range of parameters for most correlations, it is often quite difficult for a designer of a new thermal device to find a correlation that covers the entire range of all relevant parameters. Correlations are therefore sometimes applied beyond their range of validity. Such extrapolations

* Corresponding author. Tel.: +1 765 494 5705; fax: +1 765 494 0539.
E-mail address: mudawar@ecn.purdue.edu (I. Mudawar).

0017-9310/$ - see front matter © 2007 Published by Elsevier Ltd.
doi:10.1016/j.ijheatmasstransfer.2007.01.029

Nomenclature

A	cross-sectional area of channel
A_k	cross-sectional area occupied by phase k
A_w	area of wetting front
b	ratio of wetting front length to wavelength, w/λ
c	wave speed
$C_{f,i}$	interfacial friction factor
c_i	imaginary component of wave speed
$c_{p,f}$	specific heat of liquid
c_r	real component of wave speed
D_k	hydraulic diameter for phase k
f_k	wall friction factor for phase k
G	mass flux, $\rho_f U$
g_a	component of acceleration acting axially opposite to direct of fluid flow
g_e	earth's gravitational acceleration
g_n	component of acceleration normal to heated wall
H	channel height (5.0 mm)
h_b	enthalpy of bulk liquid
h_g	enthalpy of saturated vapor
h_{fg}	latent heat of vaporization
h_i	enthalpy of liquid at inlet
Δh_{sub}	enthalpy difference between saturated liquid and bulk liquid
k	wave number, $2\pi/\lambda$
k_c	critical wave number, $2\pi/\lambda_c$
L	heater length in flow direction (101.6 mm)
P	pressure
p_h	heated perimeter
p_i	interfacial perimeter between phases
p_k	perimeter of wall contact with phase k
P_o	outlet pressure
q''	wall heat flux
q''_m	critical heat flux
q''_w	wetting front lift-off heat flux
$Re_{D,k}$	Reynolds number for phase k based on phase hydraulic diameter
t	time
T	temperature
$\Delta T_{sub,o}$	outlet subcooling, $T_{sat,o} - T_{b,o}$
U	mean liquid inlet velocity
U_f	mean liquid phase velocity
U_g	mean vapor phase velocity
$U_{g,n}$	mean vapor velocity in wetting front normal to wall
W	heater and channel width (2.5 mm)
W'_{fg}	rate of interfacial evaporation per unit streamwise distance
x	flow quality
z	streamwise coordinate
z_0	streamwise distance where $U_f = U_g$
z_*	extent of continuous upstream wetting region

Greek symbols

α	void fraction, δ/H
δ	mean vapor layer thickness; vapor layer amplitude used in CHF model
η	interfacial perturbation
η_0	amplitude of interfacial perturbation, $\eta_0 = \delta$
λ	vapor wavelength
λ_c	critical wavelength
λ_j	wavelength of jth wave
μ_k	phase viscosity
ξ	heat utility ratio
ρ_f	modified liquid density
ρ_g	modified vapor density
ρ_k	density of saturated phase k
σ	surface tension
τ_i	interfacial shear stress
$\tau_{w,k}$	shear stress between wall and phase k

Subscripts

b	bulk liquid
f	saturated liquid
g	saturated vapor
i	inlet; imaginary component
k	Phase k (k = f for liquid or g for vapor)
m	maximum, critical heat flux
o	outlet
sat	saturation
w	wetting front; wall

may be quite questionable, given the great safety concerns associated with CHF determination.

To alleviate extrapolation concerns, a smaller number of studies have been focused on physical understanding of the CHF phenomenon in pursuit of a mechanistic theoretical model that may be applied to different fluids and broad ranges of the relevant parameters. Unfortunately, this is a very complex endeavor, given the limited number of photographic studies that capture the near-wall interfacial behavior that is vital to the development of such a model. Several mechanisms have been proposed to construct such models. They include *Boundary Layer Separation* [1,2], *Bubble Crowding* [3–5], *Sublayer Dryout* [6–12], and *Interfacial Lift-off* [13–20].

Very few studies have been dedicated to flow boiling in microgravity. The majority of these concern bubble behavior and two-phase heat transfer coefficient [21–25]. Microgravity flow boiling CHF data are especially rare. Ma and Chung [24] attempted to obtain such data in a 2.1 s drop tower. They generated boiling curves spanning the single-phase and nucleate boiling regions including the CHF point for three flow velocities. The authors of the present

study conducted near-saturated flow boiling CHF experiments onboard NASA's KC-135 turbojet [20]. CHF data were measured for near-saturated conditions and flow velocities from 0.1 to 1.5 m/s. CHF values were unusually small at low velocities in μg_e compared to $1g_e$, but the effect of gravity diminished greatly at high velocities. Zhang et al. also conducted extensive high-speed video imaging studies of flow boiling behavior that proved flow boiling CHF in microgravity is triggered by the Interfacial Lift-off mechanism.

A key limitation of the Interfacial Lift-off Model is its inability to tackle subcooled flows. The present study is the first attempt at extending this model to subcooled conditions. New CHF data were measured in both 1 g_e ground experiments and μg_e parabolic flight experiments. A new relation is derived to estimate the partitioning of wall heat flux between sensible and latent heat. This relation is incorporated in the original Interfacial Lift-off Model to predict data for both gravitational fields corresponding to different flow velocities and subcoolings.

2. Experimental methods

2.1. Flow boiling module

A flow boiling test module was designed to both measure flow boiling CHF and photographically capture interfacial behavior. The module consisted of two transparent polycarbonate plastic (Lexan) plates and a heater assembly. As shown in Fig. 1a, a 5.0 × 2.5 mm rectangular flow channel was milled into the underside of the top plastic plate. The heated wall consisted of a 0.56 mm thick and 101.6 mm long copper plate that was heated by a series of thick film resistors. The copper plate was sandwiched between the two plastic plates. A honeycomb flow straightener at the channel inlet and an entry length 106 times the channel hydraulic diameter ensured fully developed flow at the upstream edge of the heated wall. Two thermocouples provided fluid temperature readings just upstream and downstream of the heated wall with an uncertainty of 0.3 °C. Pressure transducers at the same locations provided pressure readings with an accuracy of 0.01%.

The heater assembly was designed to provide uniform heat flux along the surface of the copper plate. As shown in Fig. 1b, the heater assembly was formed by soldering six thick-film resistors to the underside of the copper plate. The resistors were connected in parallel to a variable voltage transformer. The heater assembly featured fast temperature response to changes in heat flux and gravitational acceleration, which is crucial for flight experiments. With the small thickness of the copper plate and small thermal mass of the resistors, the wall temperature could reach steady state in less than 5 s following a heat flux increment. The 0.56 mm thickness of the copper plate was sufficiently large to preclude any CHF dependence on copper plate thickness. A detailed discussion on the heater's temperature response is available in [20]. Wall temperature was

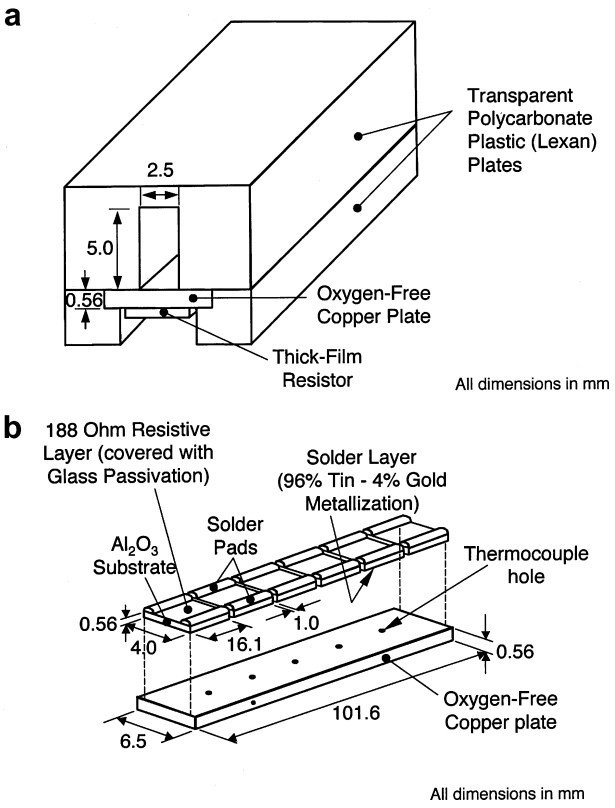

Fig. 1. (a) Flow channel assembly and (b) construction of heated wall.

measured by five thermocouples inserted in the copper plate. These thermocouples had an uncertainty of 0.3 °C. The heat flux was determined by dividing the electrical power input to the resistors by the wetted area of the heated wall. Power input was measured by a power meter, and the overall uncertainty of the heat flux measurement was 0.2 W/cm^2.

2.2. Flow loop

Fig. 2a shows a schematic diagram of the test loop. This compact two-phase flow loop was used to both deaerate the working fluid, FC-72, prior to testing and maintain desired flow conditions during the tests. Past experiments and repeatability tests by the authors have shown deaerating the fluid for about 30 min ensured the removal of any non-condensible gases from the loop. The fluid was circulated in the loop with the aid of a centrifugal pump. Flow rate was controlled by a throttling valve situated downstream of the pump. The fluid then passed through a filter, a turbine flow meter, and an in-line electric heater, before entering the flow boiling module. Exiting the module, the fluid passed through an air-cooled heat exchanger before returning to the pump. Fluid temperature was regulated by controlling the heat exchanger's fan speed and fine-tuned with the aid of the in-line electric heater. Fluid pressure downstream of the heated wall was maintained with the aid of an accumulator charged with nitrogen gas. As depicted in Fig. 2b, the entire test facility, including the

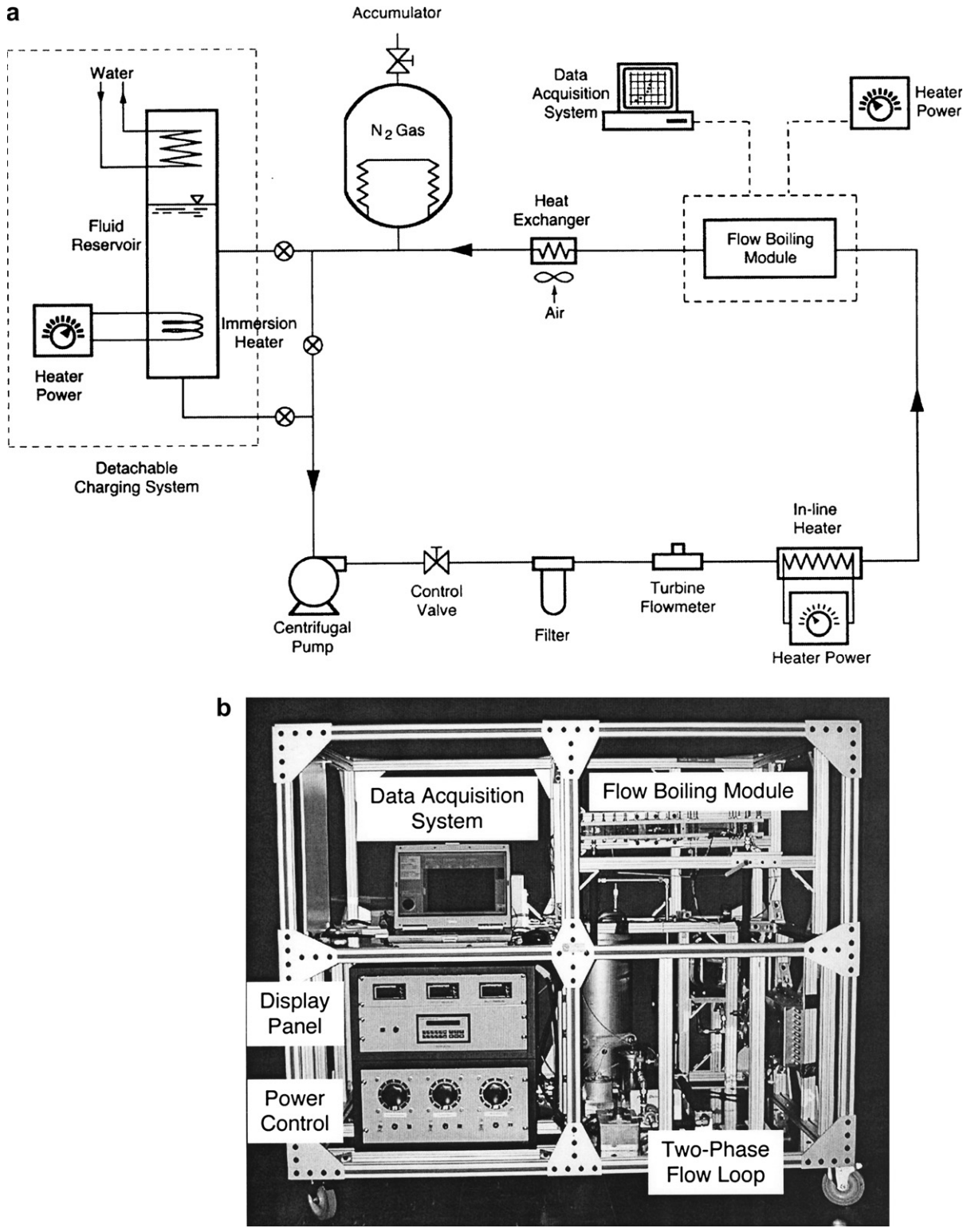

Fig. 2. (a) Schematic of two-phase flow loop and (b) photo of flight apparatus.

flow loop components, power and instrumentation cabinets, and data acquisition system, was mounted onto a rigid extruded aluminum frame.

Experiments were performed in microgravity and later repeated at 1 g_e to validate the CHF model for both environments.

2.3. Parabolic flight

The reduced gravity environment was simulated aboard a plane that flew a series of parabolic maneuvers as illustrated in Fig. 3a. Reduced gravity conditions such as microgravity, Lunar gravity (0.16 g_e) and Martian gravity

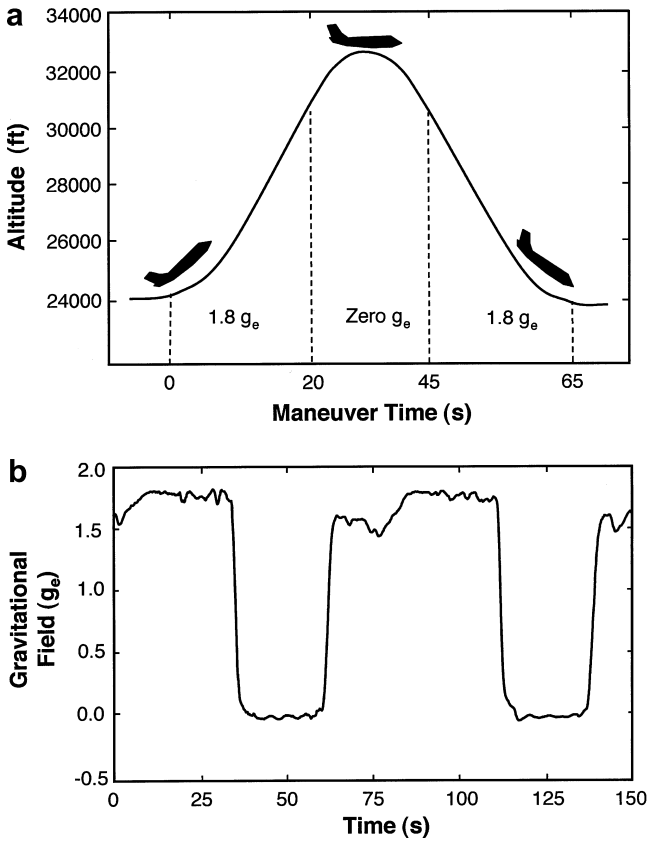

Fig. 3. (a) Trajectory and (b) gravitational change of parabolic flight.

(0.38 g_e), were achieved with different parabolic maneuvers. Fig. 3b shows the variation of gravitational acceleration recorded during microgravity experiments. During a microgravity parabola, a 23 s microgravity period was achieved between two 20 s 1.8 g_e periods. A flight mission usually consisted of 4 sets of 10 parabolas with about 5 min break between consecutive sets. Ten flight missions, about 450 parabolas, were dedicated to the present study aboard two different aircraft, NASA's KC-135 turbojet and Zero-G Corporation's Boeing 727–200.

During a parabolic flight experiment, the desired fluid flow conditions were set before each set of parabolas. Power to the heater assembly was set and maintained before pulling out from a 23 s microgravity period. The power was then increased by an increment of 1–3 W/cm^2 until a sudden unsteady rise in wall temperature was detected during a microgravity period. Flow boiling CHF in microgravity is defined as the last heat flux measured prior to the unsteady temperature rise. Besides measuring CHF, vapor behavior was monitored near the outlet of the heated wall with the aid of a high-speed video camera.

3. CHF model

The present CHF model is an extension of the Interfacial Lift-off Model first conceived by Galloway and Mudawar [13,14] for near-saturated conditions and short heated walls and later modified by Gersey and Mudawar [15,16] for longer walls. Later, Sturgis and Mudawar [17,18] observed that CHF in subcooled flow boiling was also triggered by interfacial lift-off but did not formulate a model for these conditions. They observed a periodic distribution of vapor patches along the heated surface immediately prior to CHF. Liquid replenishment of the near-wall region and cooling of the surface occurred only at discrete wetting fronts between the vapor patches. Severe vapor effusion in a wetting front lifted the vapor-liquid interface away from the surface. The formation of a continuous vapor blanket ensued and heat transfer in the remaining wetting fronts increased in order to compensate for the loss of the lifted wetting front. This caused accelerated lift-off of new wetting fronts and an appreciable unsteady rise in the wall temperature.

The authors of the present study observed the same vapor behavior for both near-saturated and subcooled flow boiling in microgravity, Fig. 4 [20]. They also successfully used the Interfacial Lift-off Model to predict flow-boiling CHF in microgravity for near-saturated flow.

In this study, the Interfacial Lift-off Model is modified to predict subcooled flow boiling CHF for both 1 g_e and μg_e conditions. As shown in Fig. 5, the vapor-liquid interface is idealized as a sinusoidal wave with amplitude and wavelength increasing in the flow direction. Due to the liquid's inlet subcooling, bubble formation is expected to occur some distance from the upstream edge of the heated wall. However, calculations of the point of bubble departure based on Levy's model [26] as well as video analysis

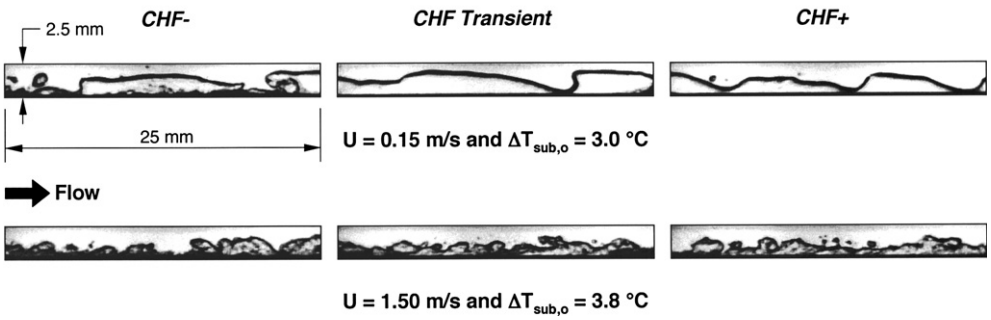

Fig. 4. CHF transient along downstream section of heated wall for near-saturated flow in μg_e at low and high velocities.

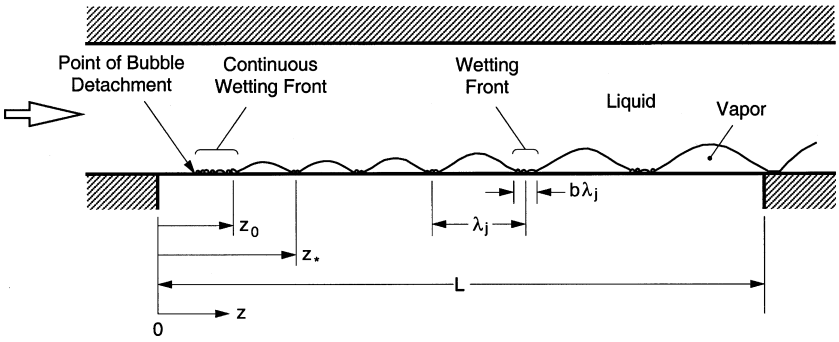

Fig. 5. Idealized wavy vapor–liquid interface with periodic wetting fronts.

showed boiling was initiated within less than 1 mm from the leading edge of the heated wall for all conditions of the present study. Fig. 5 shows an initial continuous upstream wetting front up to point z_0, followed by the formation of the first wetting front at z_*.

Like the original model, the present model consists of four sub-models that describe the liquid and vapor flows and conditions leading to interfacial lift-off. First, a separated flow model is employed to predict bulk liquid enthalpy and local mean values of liquid velocity, vapor velocity, and average vapor layer thickness. Second, an interfacial instability analysis utilizes this information to describe the spacing of wetting fronts and pressure force created by interfacial curvature. Third, the lift-off criterion is defined as the heat flux required to generate sufficient vapor momentum in the wetting fronts to overcome the pressure force exerted upon the interface due to interfacial curvature. Fourth, an energy balance is written for the heated wall relating the average surface heat flux at CHF to the heat flux concentrated in the wetting fronts. Additionally, flow visualization plays a key role in model closure by providing support for specification of the ratio of wetting front length to vapor wavelength.

Unlike the original saturated flow boiling CHF model, the sub-models introduced here are complicated by axial variations of the liquid bulk enthalpy and partitioning of wall energy between sensible and latent heat. Following are detailed derivations for all four sub-models.

3.1. Separated flow model

The present CHF model requires knowledge of bulk liquid enthalpy, liquid phase velocity, vapor phase velocity, and average vapor layer thickness as a function of axial distance. Visual observations at heat fluxes nearing CHF indicated that the two-phase mixture was, for the most part, separated over the entire length of the heater [20]. Therefore, the flow is modeled by solving the mass, momentum, and energy conservation equations using a type of separated two-phase flow model called the slip flow model. This model assumes one-dimensional flow with uniform velocity and enthalpy within each phase, while allowing for differences in the phase velocities. Furthermore, the vapor and liquid layers are assumed to be in mechanical equilibrium and, hence, pressure is uniform across the flow area at any given axial location. Additional slip flow assumptions include steady state and a uniform wall heat flux. Although the liquid–vapor interface is actually wavy, the separated flow model is quite effective in providing reliable estimates of the vapor and liquid velocities and average vapor layer thickness as a function of axial distance.

Fig. 6 provides definitions for the key geometrical parameters used in this model. Liquid is assumed to enter a rectangular channel of width W and height H at a mass velocity G. The channel is subjected to a uniform heat flux q'' along only one side. A vapor layer of thickness δ is established and grows thicker along the flow direction. Conservation relations are applied below for a channel control volume of length Δz.

The mass flow rate of liquid evaporating at the vapor-liquid interface is expressed by the mass conservation equation as

$$W'_{\mathrm{fg}} = \frac{\mathrm{d}}{\mathrm{d}z}(\rho_{\mathrm{g}} U_{\mathrm{g}} A_{\mathrm{g}}). \tag{1}$$

Introducing the mass vapor quality yields the following relations for the vapor and liquid layers, respectively,

$$x = \frac{\rho_{\mathrm{g}} U_{\mathrm{g}} A_{\mathrm{g}}}{GA} = \frac{\rho_{\mathrm{g}} U_{\mathrm{g}} \alpha}{G} \tag{2}$$

and

$$1 - x = \frac{\rho_{\mathrm{f}} U_{\mathrm{f}} A_{\mathrm{f}}}{GA} = \frac{\rho_{\mathrm{f}} U_{\mathrm{f}} (1-\alpha)}{G}, \tag{3}$$

where $\alpha = A_{\mathrm{g}}/A = \delta/H$. Combining Eqs. (1) and (2) yields

$$W'_{\mathrm{fg}} = GA\frac{\mathrm{d}x}{\mathrm{d}z}. \tag{4}$$

Applying conservation of momentum to the liquid and vapor control volumes separately results in the following equations:

$$G^2 \frac{\mathrm{d}}{\mathrm{d}z}\left[\frac{(1-x)^2}{\rho_{\mathrm{f}}(1-\alpha)}\right] = -(1-\alpha)\frac{\mathrm{d}P}{\mathrm{d}z} - \frac{\tau_{\mathrm{w,f}} p_{\mathrm{w,f}}}{A} + \frac{\tau_{\mathrm{i}} p_{\mathrm{i}}}{A} - \rho_{\mathrm{f}}(1-\alpha) g_{\mathrm{a}} \tag{5}$$

and

$$A = HW \qquad D = \frac{2HW}{H+W} \qquad p_h = W$$
$$A_f = W(H-\delta) \qquad D_f = \frac{2W(H-\delta)}{W+H-\delta} \qquad p_{w,f} = W + 2(H-\delta)$$
$$A_g = W\delta \qquad D_g = \frac{2W\delta}{W+\delta} \qquad p_{w,g} = W + 2\delta$$
$$\alpha = \frac{A_g}{A} = \frac{\delta}{H} \qquad p_i = W$$

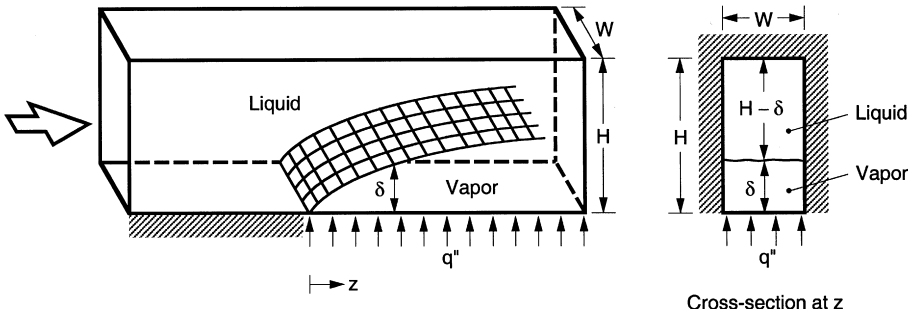

Fig. 6. Separated vapor–liquid flow in rectangular channel subjected to one-sided heating.

$$G^2 \frac{\mathrm{d}}{\mathrm{d}z}\left(\frac{x^2}{\rho_g \alpha}\right) = -\alpha \frac{\mathrm{d}P}{\mathrm{d}z} - \frac{\tau_{w,g} p_{w,g}}{A} - \frac{\tau_i p_i}{A} - \rho_g \alpha g_a, \tag{6}$$

where g_a is the component of acceleration acting axially opposite to the direction of fluid flow. Summing Eqs. (5) and (6) gives the following expression for pressure gradient,

$$-\frac{\mathrm{d}P}{\mathrm{d}z} = G^2 \frac{\mathrm{d}}{\mathrm{d}z}\left[\frac{x^2}{\rho_g \alpha} + \frac{(1-x)^2}{\rho_f (1-\alpha)}\right] + \frac{\tau_{w,g} p_{w,g} + \tau_{w,f} p_{w,f}}{A} + [\rho_g \alpha + \rho_f (1-\alpha)] g_a. \tag{7}$$

The wall shear stress in phase k (either liquid or vapor) is given by

$$\tau_{w,k} = \frac{f_k}{2} \rho_k U_k^2. \tag{8}$$

Bhatti and Shah [27] developed the following formula for the Fanning friction factor applicable to laminar, transition, and turbulent flow regimes,

$$f_k = C_1 + \frac{C_2}{Re_{D,k}^{1/C_3}}. \tag{9}$$

For laminar flow ($Re_{D,k} \leqslant 2100$), $C_1 = 0, C_2 = 16, C_3 = 1$; for transition flow ($2100 < Re_{D,k} \leqslant 4000$), $C_1 = 0.0054$, $C_2 = 2.3 \times 10^{-8}$, $C_3 = -2/3$; and for turbulent flow ($Re_{D,k} > 4000$), $C_1 = 0.00128$, $C_2 = 0.1143$, $C_3 = 3.2154$. The Reynolds number for phase k is based on the hydraulic diameter,

$$Re_{D,k} = \frac{\rho_k U_k D_k}{\mu_k}. \tag{10}$$

The interfacial shear stress on the liquid by the vapor is defined as

$$\tau_i = \frac{C_{f,i}}{2} \rho_g (U_g - U_f)^2 \tag{11}$$

Both Galloway and Mudawar [14] and Gersey and Mudawar [16] critiqued several models for the interfacial friction coefficient, $C_{f,i}$, and recommended a constant value of 0.5 for a wavy vapor–liquid interface.

The energy conservation equation yields an expression for the local bulk liquid enthalpy at any axial location z:

$$\frac{q'' p_h}{GA} = \frac{\mathrm{d}}{\mathrm{d}z}[x h_g + (1-x) h_b], \tag{12}$$

Integrating Eq. (12) gives the following expression for bulk liquid enthalpy,

$$h_b(z) = \frac{h_i - x(z) h_g(z) + \frac{q'' p_h}{GA} z}{1 - x(z)}, \tag{13}$$

If a heat utility ratio given by ξ is defined as the fraction of the surface heat flux that converts stagnant, near-wall liquid at the local bulk temperature to vapor, then

$$W'_{fg}[h_{fg}(z) + \Delta h_{sub}(z)]\mathrm{d}z = \xi q'' p_h \, \mathrm{d}z, \tag{14}$$

where Δh_{sub} is the difference between the saturated enthalpy and local bulk liquid enthalpy. Substitution of Eq. (4) into Eq. (14) yields

$$\frac{\mathrm{d}x}{\mathrm{d}z} = \frac{\xi q'' p_h}{GA[h_{fg}(z) + \Delta h_{sub}(z)]}. \tag{15}$$

Assuming the heat utility ratio, ξ, is known, the mass, momentum, and energy equations can be expressed in terms of four independent variables: α (or δ), x, h_b, and P. All other parameters (e.g. U_f and U_g) can be expressed in terms of these variables. Thermophysical properties in the liquid are determined by the local bulk liquid temperature and therefore h_b. Saturated thermophysical properties of the liquid and vapor are determined by the local pressure, P. The model equations are solved simultaneously to determine the variations of δ, x, h_b, and P relative to z. The mean liquid velocity, U_f, and mean vapor velocity, U_g, are determined thereafter from these four independent

variables. The heat utility ratio, ξ, required for this solution is discussed later.

3.2. Interfacial instability analysis

The periodic, wavy interface between the vapor and liquid prior to CHF resembles the classical case shown in Fig. 7a of two fluids moving relative to each other between two infinite parallel walls. Disturbances may lead to an unstable interface and the objective is to find the wavelength for which the interface is neutrally stable; that is, on the verge of becoming unstable. An interface having this critical wavelength would be most susceptible to the momentum flux of vapor emanating from the wetting fronts. The critical wavelength is obviously a function of the mean liquid velocity, U_f, mean vapor velocity, U_g, and the average vapor layer thickness, δ, quantities determined from the separated flow model.

Assuming that a disturbance produces a sinusoidal interface,

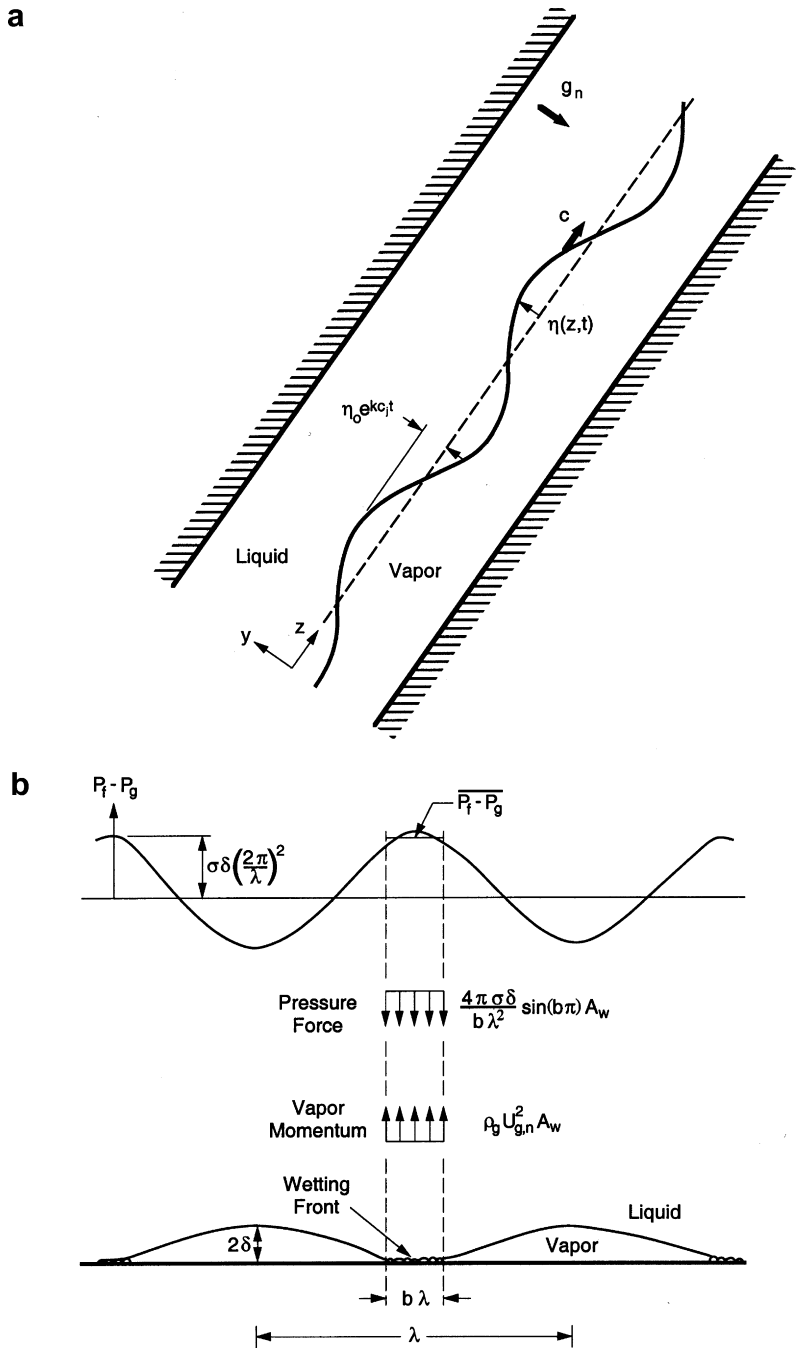

Fig. 7. (a) Idealized sinusoidal liquid–vapor interface and (b) vapor momentum and interfacial pressure difference used to determine lift-off heat flux (adapted from Zhang et al. [20]).

$$\eta(z,t) = \eta_0 e^{ik(z-ct)}, \tag{16}$$

the pressure rise across the interface can be expressed as

$$P_f - P_g = -\left[\rho_f''(c-U_f)^2 + \rho_g''(c-U_g)^2 + (\rho_f - \rho_g)\frac{g_n}{k}\right]k\eta, \tag{17}$$

where $k = 2\pi/\lambda$ is the wave number, c is the wave speed, $\rho_f^* = \rho_f \coth(kH_f)$, and $\rho_g^* = \rho_g \coth(kH_g)$. Alternatively, a two-dimensional interface with small curvature has an approximate pressure difference of

$$P_f - P_g \approx \sigma\frac{\partial^2\eta}{\partial z^2} = -\sigma k^2\eta. \tag{18}$$

Equating pressure difference in Eqs. (17) and (18) yields an expression for the wave speed:

$$c = \frac{\rho_f'' U_f + \rho_g'' U_g}{\rho_f'' + \rho_g''} \pm \sqrt{\frac{\sigma k}{\rho_f'' + \rho_g''} - \frac{\rho_f''\rho_g''(U_g - U_f)^2}{(\rho_f'' + \rho_g'')^2} - \frac{(\rho_f - \rho_g)}{(\rho_f'' + \rho_g'')}\frac{g_n}{k}}, \tag{19}$$

where g_n is the component of acceleration perpendicular to the heated wall. The first term within the radical in Eq. (19) accounts for the effect of surface tension and is always stabilizing. The second term results from the velocity difference between the phases and is always destabilizing. The last term can be either stabilizing or destabilizing depending upon the orientation of the interface with respect to the gravitational field. If the argument within the radical in Eq. (19) is positive, the wave speed is real, and the interface is sinusoidal, stable, and diminishing in amplitude. Allowing for a negative argument results a complex wave speed, $c = c_r + ic_i$. The imaginary component of this wave speed is

$$c_i = \sqrt{\frac{\rho_f''\rho_g''(U_g - U_f)^2}{(\rho_f'' + \rho_g'')^2} + \frac{(\rho_f - \rho_g)}{(\rho_f'' + \rho_g'')}\frac{g_n}{k} - \frac{\sigma k}{\rho_f'' + \rho_g''}}. \tag{20}$$

The existence of an imaginary component signifies an unstable interface. Neutral stability occurs when $c_i = 0$. Setting Eq. (20) equal to zero and solving for k yields the following expression for the critical wavelength, λ_c,

$$k_c = \frac{2\pi}{\lambda_{cr}} = \frac{\rho_f''\rho_g''(U_g - U_f)^2}{2\sigma(\rho_f'' + \rho_g'')} + \sqrt{\left[\frac{\rho_f''\rho_g''(U_g - U_f)^2}{2\sigma(\rho_f'' + \rho_g'')}\right]^2 + \frac{(\rho_f - \rho_g)g_n}{\sigma}}. \tag{21}$$

3.3. Interfacial lift-off criterion

The present model postulates that the liquid–vapor interface be lifted away from the heated wall when the momentum flux of vapor emanating from the wetting front exceeds the pressure force acting upon the interface due to the interface curvature. The heat flux causing interfacial lift-off may be found by equating the average pressure force acting to maintain interfacial contact and the vapor momentum tending to push the interface away from the surface as illustrated in Fig. 7b. Integrating Eq. (18) over the length $\ell = b\lambda$ of the wetting front and dividing the result by this length yields the average pressure difference for the wetting front:

$$\overline{P_f - P_g} = \frac{4\pi\sigma\delta}{b\lambda_c^2}\sin(\pi b). \tag{22}$$

The heat flux, q_w'', dedicated to converting a mass of subcooled liquid into saturated vapor at a wetting front can be expressed as

$$q_w'' A_w = (h_{fg} + \Delta h_{sub})\rho_g U_{g,n} A_w, \tag{23}$$

Table 1
Present $1g_e$ horizontal flow boiling CHF data

$\Delta T_{sub,o} = 3 \pm 2$ °C		$\Delta T_{sub,o} = 10 \pm 2$ °C		$\Delta T_{sub,o} = 20 \pm 2$ °C		$\Delta T_{sub,o} = 30 \pm 2$°C	
U (m/s)	CHF (W/cm^2)	U (m/s)	CHF (W/cm^2)	U (m/s)	CHF (W/cm^2)	U (m/s)	CHF (W/cm^2)
0.10	27.6	0.5	30.1	0.5	31.6	0.5	34.6
0.19	29.0	0.8	31.3	0.8	33.7	0.8	38.6
0.28	30.4	1.0	31.9	1.0	35.2	1.0	40.9
0.31	31.0	1.2	32.5	1.2	37.4	1.2	43.2
0.46	29.0	1.5	33.1	1.5	40.3	1.5	46.7
0.48	31.3						
0.54	30.8						
0.80	31.0						
0.90	30.1						
0.90	29.2						
1.10	30.0						
1.30	30.9						
1.31	30.2						
1.35	31.3						
1.50	30.3						

Table 2
Present μg_e CHF data

$\Delta T_{sub,o} = 4 \pm 2$ °C		$\Delta T_{sub,o} = 8 \pm 2$ °C		$\Delta T_{sub,o} = 32 \pm 2$ °C	
U (m/s)	CHF (W/cm^2)	U (m/s)	CHF (W/cm^2)	U (m/s)	CHF (W/cm^2)
0.10	10.1	0.10	14.0	0.30	21.2
0.15	13.8	0.16	13.9	0.50	23.0
0.19	14.6	0.24	14.5	0.60	24.9
0.23	14.0	0.29	17.5	0.70	26.0
0.25	15.4	0.30	18.1	1.10	30.5
0.26	15.0	0.31	20.4	1.50	35.2
0.90	23.2	0.46	20.6		
1.10	25.5	0.48	22.3		
1.50	28.7	0.53	22.8		
		0.80	27.2		
		0.90	25.0		
		1.30	26.3		
		1.31	27.3		
		1.35	27.8		

Table 3
Sturgis and Mudawar [17,18] 1g_e horizontal flow boiling CHF data

$\Delta T_{sub,o} = 3$ °C		$\Delta T_{sub,o} = 16$ °C		$\Delta T_{sub,o} = 29$ °C	
U (m/s)	CHF (W/cm^2)	U (m/s)	CHF (W/cm^2)	U (m/s)	CHF (W/cm^2)
0.5	25.1	0.5	35.2	0.5	42.7
0.5	24.9	0.5	35.5	0.5	43.1
1.0	28.2	1.0	38.8	1.0	48.8
1.5	30.5	1.0	38.3	1.0	48.4
2.0	31.3	1.5	41.8	1.5	54.0
2.0	32.9	1.5	42.0	1.5	51.5
3.0	34.3	2.0	44.3	1.5	51.2
3.0	34.8	2.0	44.0	2.0	59.4
3.0	34.7	2.0	42.8	3.0	70.7
4.0	36.8	3.0	47.0	3.0	73.6
5.0	36.5	4.0	52.4	4.0	86.9
5.0	36.5	4.0	51.8	5.0	97.1
6.0	37.8	5.0	63.1	6.0	108.7
7.0	42.3	6.0	71.7	7.0	118.2
8.0	46.9	6.0	69.3	8.0	129.3
		7.0	76.6		
		7.0	76.4		
		8.0	85.8		

where A_w is the surface area associated with the wetting front and $U_{g,n}$ the vapor velocity normal to the surface.

Equating the vapor momentum flux per unit area, $\rho_g U_{g,n}^2$, to the average pressure difference, the local lift-off heat flux at the downstream edge of the heat wall can be determined as

$$q''_w = \rho_g(h_{fg} + c_{p,f}\Delta T_{sub,o})\left(\frac{P_f - P_g}{\rho_g}\right)^{1/2} = \rho_g(h_{fg} + c_{p,f}\Delta T_{sub,o})\left(\frac{4\pi\sigma\delta}{\rho_g b\lambda_c^2}\sin(\pi b)\right)^{1/2} \quad (24)$$

A statistical examination of interfacial waves by Zhang et al. [19] showed that, just prior to CHF, waves generated at z_* have a tendency to preserve their curvature as they propagate downstream. CHF then ensues when the most downstream wetting front begins lifting from the heated wall near $z = L$. Therefore δ and λ_c in Eq. (24) are evaluated at z_*, which is defined as $z_* = z_0 + \lambda_c(z_*)$, where z_0 is the location at which the vapor velocity just exceeds the liquid velocity, both of which are determined from the separated flow model.

3.4. Energy balance

Zhang et al. [19] showed that the interfacial wavelength and the wetting front length increase in the flow direction but the wetting front length remains a constant fraction of the local wavelength with $b = 0.20$. Prior to CHF, liquid is converted into vapor only in the wetting fronts. The portion, ξ, of the wall heat flux at CHF, q''_m, that is dedicated to vapor generation is related to the localized lift-off heat flux by

$$\xi q''_m = b q''_w. \quad (25)$$

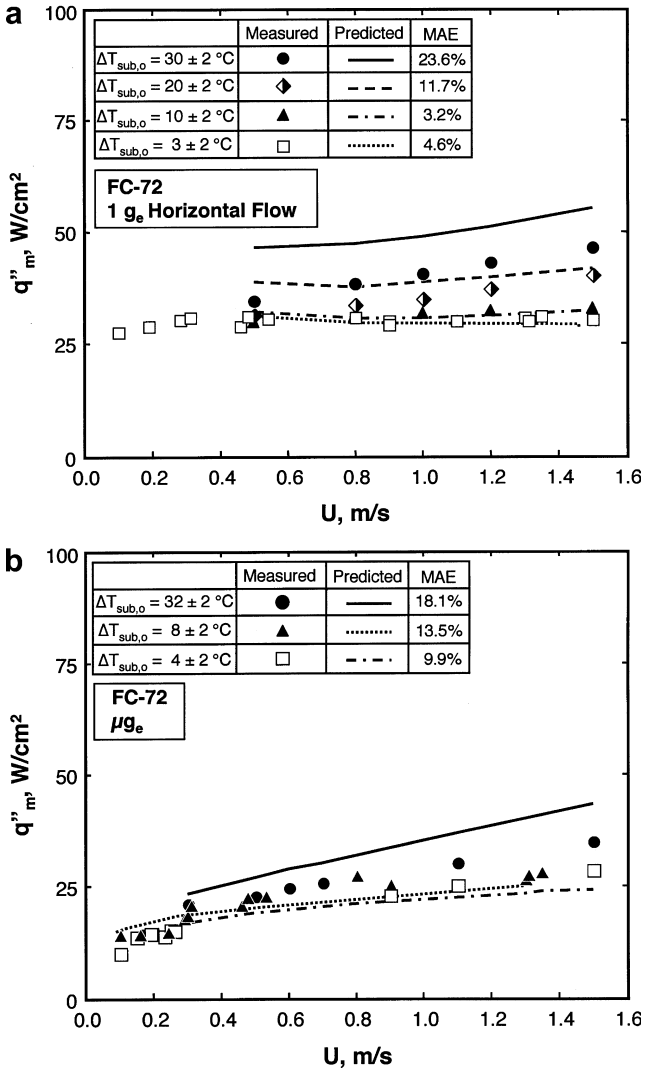

Fig. 8. Comparison of model predictions and present data measured at (a) 1 g_e and (b) μg_e.

Combining Eqs. (24) and (25) yields the following expression for CHF,

$$q''_{\mathrm{m}} = \frac{b}{\xi}\rho_{\mathrm{g}}(h_{\mathrm{fg}} + c_{p,\mathrm{f}}\Delta T_{\mathrm{sub,o}})\left[\left(\frac{4\pi\sigma\delta}{\rho_{\mathrm{g}} b\lambda_c^2}\sin(\pi b)\right)\bigg|_{z_*}\right]^{1/2}. \quad (26)$$

4. Model assessment

The present model was developed to predict CHF for flow boiling with different outlet subcoolings at 1 g_e and μg_e. To validate this model, CHF values were measured for FC-72 in both ground and parabolic flight experiments. In the ground experiments, the channel was mounted horizontally with the heated wall of the channel facing Earth's gravity (i.e. $g_a = 0$ and $g_n = 1\ g_e$). The measured 1 g_e CHF data are given in Table 1 and include outlet subcooling of 3, 10, 20, and 30 °C corresponding to an outlet pressure of $P_o = 1.44 \times 10^5$ Pa (20.9 psi). CHF values measured at μg_e ($g_a = g_n = 0$) are listed in Table 2 and correspond to the same outlet pressure as the 1 g_e data. Sturgis and Mudawar [17,18] previously performed horizontal flow boiling CHF experiments with FC-72 at 1 g_e in which the heated wall was vertically mounted (i.e. $g_a = g_n = 0$). Their channel had the same geometry and dimensions as the present study but a much thicker heated wall. Their data were obtained at an outlet pressure of 1.38 bars (20 psi) over a velocity range of 0.25–10 m/s and outlet subcoolings of 3, 16, and 29 °C. Listed in Table 3, the Sturgis and Mudawar CHF data provided added opportunity for validation of the present model.

As indicated earlier, solution of the separated flow model conservation relations and determination of the lift-off heat flux require knowledge of the magnitude of the heat utility ratio, ξ. Information regarding this important parameter is very hard to track. Rohsenow [28] postulated that heat transfer of subcooled flow boiling is the superposition of the heat transferred by single-phase convection and the heat transferred by bubble nucleation. Levy [29], Gambill [30], Avksentyuk [31], and Siman-Tov et al. [32] assumed that subcooled flow boiling CHF is the superposition of the heat flux transferred by single-phase forced convection and the heat flux corresponding to subcooled pool boiling. These studies suggest that only a portion of the wall heat flux is dedicated to vapor generation during subcooled flow boiling even when CHF occurs.

As discussed earlier, the present study defines the heat utility ratio, ξ, as the fraction of the wall heat flux that converts near-wall liquid at local bulk liquid temperature to vapor. Two key criteria concerning the magnitude of this parameter are $0 \leqslant \xi \leqslant 1$ for subcooled flow, and $\xi = 1$ for saturated flow. A dimensionless relation that satisfies both criteria was derived from data obtained in the present study as well as those of Sturgis and Mudawar by minimizing least mean absolute error (MAE) in CHF prediction using the CHF model described above:

$$\xi = 1 - \frac{\rho_{\mathrm{f}}}{\rho_{\mathrm{g}}}\frac{c_{p\mathrm{f}}\Delta T_{\mathrm{sub,o}}}{h_{\mathrm{fg}}}\left[0.00285\left(\frac{\rho_{\mathrm{f}} U^2 D}{\sigma}\right)^{0.2}\right]. \quad (27)$$

Fig. 8a compares predictions of the CHF model with the present 1g_e CHF data for four outlet subcoolings. The CHF model captures all the important data trends, increasing CHF with increasing subcooling and/or velocity, and a weakening effect of velocity on CHF with decreased subco-

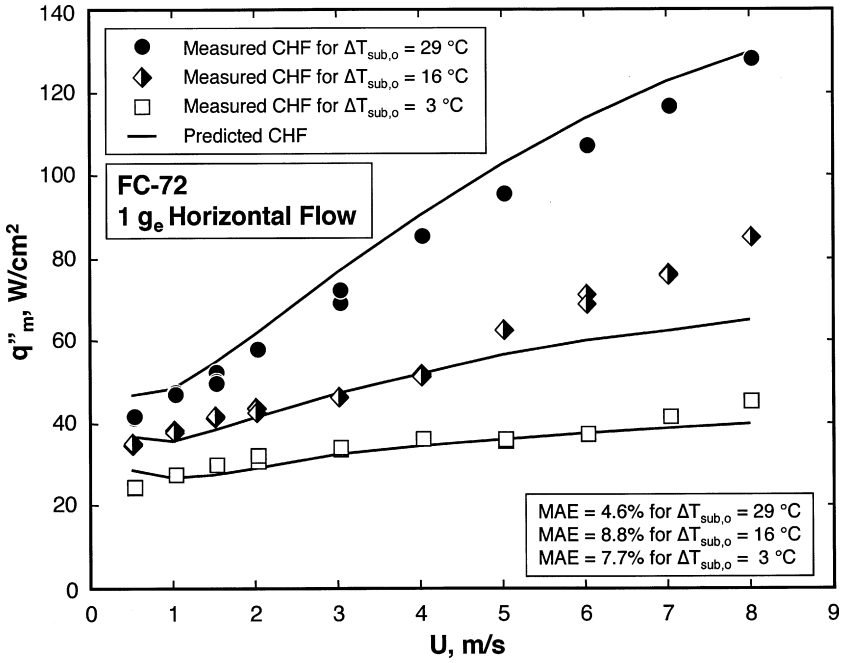

Fig. 9. Comparison of model predictions with 1 g_e CHF data measured by Sturgis and Mudawar [17,18].

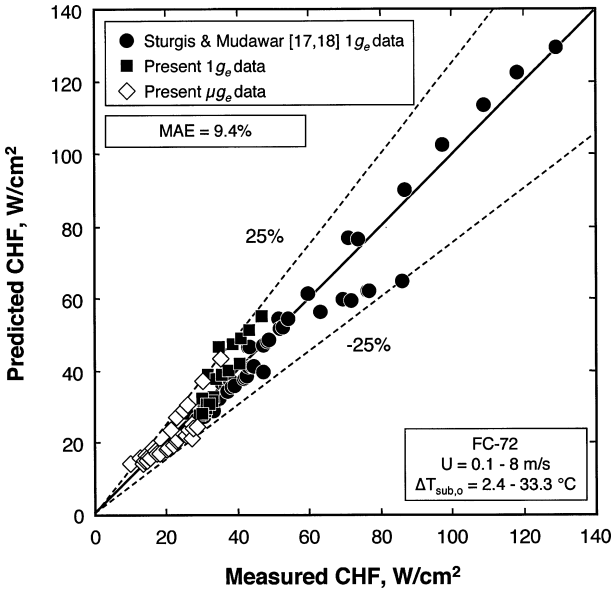

Fig. 10. Comparison of model predictions and CHF data measured at 1 g_e and μg_e.

oling. The model over-predicts the data for $\Delta T_{sub,o} = 20$ and 30 °C but provides excellent results for $\Delta T_{sub,o} = 3$ and 10 °C. However, good overall predictive ability is evidenced by the MAE for the individual subcoolings ranging from 3.2% to 23.6%. Notice that the model predictions exclude very low velocities where flow boiling resembles pool boiling rather than the wavy vapor regime upon which the present model is based.

Fig. 8b shows a similar comparison of the model predictions with the present microgravity data for three outlet subcoolings. The model over-predicts the CHF data for $\Delta T_{sub,o} = 32$ °C but provides very good predictions for $\Delta T_{sub,o} = 4$ and 8 °C. However, good overall predictive capability is shown for these μg_e data as well with the MAE for individual subcoolings ranging from 9.9% to 18.1%.

Fig. 9 shows the model accurately predicts the Strugis and Mudawar 1 g_e CHF data for all velocities and oulet subcoolings. The MAE of the model predictions is 7.7%, 8.8% and 4.6% for $\Delta T_{sub,o} = 3$, 16 and 29 °C, respectively.

To further illustrate both the accuracy and the versatility of the present model at predicting CHF data for both 1 g_e and μg_e and both near-saturated and subcooled flow, the three afore-mentioned databases are compared to the model predictions in Fig. 10. Virtually all data fall within ±25% of the model predictions and the MAE for the combined database is 9.4%.

5. Conclusions

This study extended the Interfacial Lift-off Model originally derived for saturated flow boiling CHF to subcooled flow boiling. New CHF data were measured in 1 g_e ground tests and μg_e tests performed in parabolic flight trajectory. The new database included broad variations of both flow velocity and outlet subcooling and served to validate the extended CHF model. Key findings from this study are as follows:

(1) Experimental methods, especially heated wall design, were developed that yielded reliable subcooled flow boiling CHF data in both Earth gravity and microgravity. These experimental methods also featured high-speed video imaging and analysis of the liquid–vapor interface during the CHF transient. Both the CHF data and the video records played a vital role in constructing and validating the extended CHF model.
(2) A heat utility ratio function was correlated from data obtained in the present and earlier studies to account for the partitioning of wall energy between sensible and latent heat. This function enables the application of the Interfacial Lift-of Model to subcooled flow boiling at both μg_e and 1 g_e.
(3) The new extended Interfacial Lift-off Model is very effective at predicting both near-saturated and subcooled flow boiling CHF at 1 g_e and μg_e.
(4) Future studies should address conditions that yield a substantial inlet non-boiling region. Different point of net vapor generation models could be easily incorporated into the present CHF model to extend its applicability to other fluids and operating conditions.

Acknowledgements

The authors are grateful for the support of the National Aeronautics and Space Administration under Grant No. NNC04GA54G. Several individuals provided valuable assistance in preparing the apparatus for the flight experiments and obtaining flight data. The authors especially thank John McQuillen, Kirk Logsoon and James Withrow of the NASA Glenn Center for their assistance.

References

[1] S.S. Kutateladze, A.I. Leont'ev, Some applications of the asymptotic theory of the turbulent boundary layer, in: Proceedings of Third International Heat Transfer Conference, Chicago, Illinois, 1966.
[2] L.S. Tong, Boundary-layer analysis of the flow boiling crisis, Int. J. Heat Mass Transfer 11 (1968) 1208–1211.
[3] J. Weisman, B.S. Pei, Prediction of critical heat flux in flow boiling at low qualities, Int. J. Heat Mass Transfer 26 (1983) 1463–1477.
[4] S.H. Ying, J. Weisman, Prediction of the critical heat flux in flow boiling at intermediate qualities, Int. J. Heat Mass Transfer 29 (1986) 1639–1648.
[5] J. Weisman, S. Ileslamlou, A phenomenological model for prediction of critical heat flux under highly subcooled conditions, Fusion Technol. 13 (1988) 654–659.
[6] C.H. Lee, I. Mudawar, A mechanistic critical heat flux model for subcooled flow boiling based on local bulk flow conditions, Int. J. Multiphase Flow 14 (1989) 711–728.
[7] W.S. Lin, C.H. Lee, B.S. Pei, An improved theoretical critical heat flux model for low-quality flow, Nuclear Technol. 88 (1989) 294–306.

[8] Y. Katto, A physical approach to critical heat flux of subcooled flow boiling in round tubes, Int. J. Heat Mass Transfer 33 (1990) 611–620.
[9] Y. Katto, Prediction of critical heat flux of subcooled flow boiling in round tubes, Int. J. Heat Mass Transfer 33 (1990) 1921–1928.
[10] Y. Katto, A prediction model of subcooled water flow boiling CHF for pressure in the range 0.1–20 MPa, Int. J. Heat Mass Transfer 35 (1992) 1115–1123.
[11] G.P. Celata, M. Cumo, A. Mariani, M. Simoncini, G. Zummo, Rationalization of existing mechanistic models for the prediction of water subcooled flow boiling critical heat flux, Int. J. Heat Mass Transfer 37 (1994) 347–360.
[12] G.P. Celata, M. Cumo, Y. Katto, A. Mariani, Prediction of the critical heat flux in water subcooled flow boiling using a new mechanistic approach, Int. J. Heat Mass Transfer 42 (1999) 1457–1466.
[13] J.E. Galloway, I. Mudawar, CHF mechanism in flow boiling from a short heated wall-part 1. Examination of near-wall conditions with the aid of photomicrography and high-speed video imaging, Int. J. Heat Mass Transfer 36 (1993) 2511–2526.
[14] J.E. Galloway, I. Mudawar, CHF mechanism in flow boiling from a short heated wall-part 2. Theoretical CHF model, Int. J. Heat Mass Transfer 36 (1993) 2527–2540.
[15] C.O. Gersey, I. Mudawar, Effects of heater length and orientation on the trigger mechanism for near-saturated flow boiling critical heat flux – I. Photographic study and statistical characterization of the near-wall interfacial features, Int. J. Heat Mass Transfer 38 (1995) 629–641.
[16] C.O. Gersey, I. Mudawar, Effects of heater length and orientation on the trigger mechanism for near-saturated flow boiling critical heat flux – II. Critical heat flux model, Int. J. Heat Mass Transfer 38 (1995) 643–654.
[17] J.C. Sturgis, I. Mudawar, Critical heat flux in a long, rectangular channel subjected to one-sided heating – I. Flow visualization, Int. J. Heat Mass Transfer 42 (1999) 1835–1847.
[18] J.C. Sturgis, I. Mudawar, Critical heat flux in a long, rectangular channel subjected to one-sided heating – II. Analysis of critical heat flux data, Int. J. Heat Mass Transfer 42 (1999) 1849–1862.
[19] H. Zhang, I. Mudawar, M.M. Hasan, Experimental and theoretical study of orientation effects on flow boiling CHF, Int. J. Heat Mass Transfer 45 (2002) 4463–4477.
[20] H. Zhang, I. Mudawar, M.M. Hasan, Flow boiling CHF in microgravity, Int. J. Heat Mass Transfer 48 (2005) 3107–3118.
[21] M. Saito, N. Yamaoka, K. Miyazaki, M. Kinoshita, Y. Abe, Boiling two-phase flow under microgravity, Nucl. Eng. Des. 146 (1994) 451–461.
[22] Y. Ma, J.N. Chung, An experimental study of forced convection boiling in microgravity, Int. J. Heat Mass Transfer 41 (1998) 2371–2382.
[23] Y. Ma, J.N. Chung, A study of bubble dynamics in reduced gravity forced-convection boiling, Int. J. Heat Mass Transfer 44 (2001) 399–415.
[24] Y. Ma, J.N. Chung, An experimental study of critical heat flux (CHF) in microgravity forced-convection boiling, Int. J. Multiphase Flow 27 (2001) 1753–1767.
[25] H. Ohta, Experiments on microgravity boiling heat transfer by using transparent heaters, Nucl. Eng. Des. 175 (1997) 167–180.
[26] S. Levy, Forced convection subcooled boiling – prediction of vapor volumetric fraction, Int. J. Heat Mass Transfer 10 (1967) 951–965.
[27] M.S. Bhatti, R.K. Shah, Turbulent and transition flow convective heat transfer in ducts, in: S. Kakac, R.K. Shah, W. Aung (Eds.), Handbook of Single-phase Convective Heat Transfer, John Wiley & Sons, New York, 1987.
[28] W.M. Rohsenow, A method of correlating heat transfer data for surface boiling liquids, Trans. ASME 74 (1952) 969–978.
[29] S. Levy, Prediction of the critical heat flux in forced convection flow, GEAP-3961, General Electric Co., San Jose, CA, 1962.
[30] W.R. Gambill, Generalized prediction of burnout heat flux for flowing, subcooled, wetting liquids, Chem. Eng. Prog. Symp. Ser. 59 (1963) 71–87.
[31] B.P. Avksentyuk, Critical feat fluxes with forced flow of subcooled and saturated liquids, Therm. Eng. 35 (1988) 694–697.
[32] M. Siman-Tov, W.R. Gambill, W.R. Nelson, A.E. Ruggles, G.L. Yoder, Thermal-hydraulic correlations for the advanced neutron source reactor fuel element design and analysis, in: Y.A. Hassan, L.E. Hochreiter (Eds.), Nuclear Reactor Thermal-hydraulics, ASME HTD, vol. 190, 1991, pp. 63–78.